Propagation of a short-pulse laser-driven electron beam in matter

L. Volpe, D. Batani, G. Birindelli, A. Morace, P. Carpeggiani, M. H. Xu, F. Liu, Y. Zhang, Z. Zhang, X. X. Lin, F. Liu, S. J. Wang, P. F. Zhu, L. M. Meng, Z. H. Wang, Y. T. Li, Z. M. Sheng, Z. Y. Wei, J. Zhang, J. J. Santos, and C. Spindloe

Citation: Physics of Plasmas (1994-present) **20**, 033105 (2013); doi: 10.1063/1.4793453
View online: http://dx.doi.org/10.1063/1.4793453
View Table of Contents: http://scitation.aip.org/content/aip/journal/pop/20/3?ver=pdfcov
Published by the AIP Publishing

PHYSICS OF PLASMAS 20, 033105 (2013)

Propagation of a short-pulse laser-driven electron beam in matter

L. Volpe,[1,2] D. Batani,[2] G. Birindelli,[1] A. Morace,[1] P. Carpeggiani,[1] M. H. Xu,[3] F. Liu,[1,3] Y. Zhang,[3] Z. Zhang,[3] X. X. Lin,[3] F. Liu,[2,3] S. J. Wang,[3] P. F. Zhu,[3] L. M. Meng,[3] Z. H. Wang,[3] Y. T. Li,[3] Z. M. Sheng,[3] Z. Y. Wei,[3] J. Zhang,[3] J. J. Santos,[2] and C. Spindloe[1,4]
[1]*University of Milano-Bicocca, Dipartimento di Fisica, Piazza della Scienza 3, Milano 20126, Italy*
[2]*University of Bordeaux, CNRS, CEA, CELIA (Centre Lasers Intenses et Applications), UMR 5107, F-33405 Talence, France*
[3]*Institute of Physics, Chinese Academy of Sciences, P.O. Box 603, Beijing 100080, China*
[4]*Rutherford Appleton Laboratory, HSIC, Didcot, Oxon OX11 0QX, United Kingdom*

(Received 31 July 2012; accepted 31 January 2013; published online 14 March 2013)

We studied the transport of an intense electron beam produced by high intensity laser pulses through metals and insulators. Targets were irradiated at two different intensities, 10^{17} W/cm^2 and 10^{19} W/cm^2, at the laser facility Xtreme Light XL-III in Beijing, a Ti:Sa laser source emitting 40 fs pulses at 800 nm. The main diagnostic was $Cu-K_\alpha$ fluorescence imaging. Images of K_α spots have been collected for those two laser intensities, for different target thickness, and for different materials. Experimental results are analyzed taking into account both collisional and collective effects as well as refluxing at the edge of the target. The target temperature is evaluated to be $T_c \sim 6$ eV for intensity $I = 10^{17}$ W/cm^2 (for all the tested materials: plastic, aluminium, and copper), and $T_c \sim 60$ eV in aluminium and 120 eV in titanium for intensity $I = 10^{19}$ W/cm^2. © *2013 American Institute of Physics*. [http://dx.doi.org/10.1063/1.4793453]

I. INTRODUCTION

The knowledge of the physics of fast electron transport in matter is crucial in order to assess the feasibility of the fast ignition approach to inertial confinement fusion.[1] Indeed, fast ignition depends on the generation of hot electrons, their collimation, transport, and energy deposition in the over-dense region of the plasma.[2,3] Fast electron transport is important also for other applications, such as proton acceleration via laser matter interaction[4] and warm dense matter (WDM) generation via isochoric heating.[5] The estimation of range and divergence of the electron beam in matter and in plasmas is, therefore, extremely important. In the last 10 years, many papers have been devoted to the study of fast electron transport; this included the study of propagation in metals,[6–8] insulators,[9–11] shocked materials,[12,13] foams,[14] gas,[15] and cylindrically compressed targets.[16]

In this paper, we present the results of experiments performed at the laser facility "Xtreme Light XL-III" of the Institute of Physics of the Chinese Academy of Sciences in Beijing.[17] The aim of these experiments was to investigate the production and propagation of fast electrons accelerated by a 40 fs laser pulse focused on solid targets at intensities $I \sim 10^{17}$ W/cm^2 (first run) and $I \sim 10^{19}$ W/cm^2 (second run). The used targets were of (1) different materials (plastic, aluminium, copper, and titanium) to investigate the role of density and electric conductivity on fast electron transport and (2) different thicknesses (from 1 to 70 μm) to measure stopping range and divergence of the electron beam distribution.

Fast electron generation at 10^{19} W/cm^2 has been studied in several experiments in the context of fast ignition. Instead this is far less known at 10^{17} W/cm^2, an intensity which is interesting because it corresponds to the ps-pedestal of ultra-high-intensity laser pulses. In addition, in our work the interactions at 10^{19} W/cm^2 and 10^{17} W/cm^2 are studied with the same laser thereby removing all the possible variations due to different systems.

At intensities of 10^{17} W/cm^2 and 10^{19} W/cm^2 we produce different states of matter, the irradiated target can be partially or completely ionized with a background temperature varying from few eV, corresponding to 10%–20% of target ionization (10^{17} W/cm^2) to hundred eV, corresponding to almost full ionization (10^{19} W/cm^2). The fast electron transport in cold and ionized matter, in this intensity range, is governed by two type of effects: (1) *collisional*, which are represented through stopping power, and (2) *collective*, which are produced by strong self-generated electric and magnetic fields. The impact of collective effects on fast electron propagation at 10^{19} W/cm^2 has been observed in previous works.[8,9,12,13,18,19] However, at lower intensities, the impact of collective effects is not so clear. In this paper, we clearly show that collective effects are important even at 10^{17} W/cm^2 (depending on the kind of target).

Another important consequence of the electric effects appears when the fast electron penetration range is larger than the target thickness (thin foils). In these conditions, the fast electron beam is "reflected" back into the target by the strong electric field which is generated at the edge of the target. Since the electric field is generated on both sides of the target, the fast electron beam is confined in the target until it completely loses its energy. The concept of electron refluxing was introduced for the first time by Key *et al.*[6] and Wharton *et al.*[7] (one of the first experimental evidences was given in Ref. 20). As shown in recent works,[21,22] electron refluxing makes more difficult to estimate the electron beam properties, such as its total number of electrons, their range, and their angular spread. Indeed, the obtained signals may vary in space and in intensity depending on the target geometry and on the electron beam energy. Recently, we have developed a 2D model describing fast electron propagation in matter when resistive effects and electron refluxing are important[23] (the model is based on the extension of previous works[8,24,25]). It includes collisional and collective effects at the same time. Collisional effects are dominant at intensities $I < 10^{17}$ W/cm^2. As the intensity increases, collective effects become more and more important until, for $I > 10^{19}$ W/cm^2, they dominate over collisional ones. Using such model to analyze our experimental data we evaluate a conversion efficiency from laser energy to fast electron energy of the order of 5% for intensity of 10^{17} W/cm^2, which corresponds to an electron temperature $T \sim 75$ keV, and of the order of 20% for 10^{19} W/cm^2, which corresponds to an electron temperature $T \sim 1$ MeV.

II. EXPERIMENTAL SET-UP AND LASER SYSTEM

The experiments have been performed with the "Xtreme Light XL-III" laser facility at the Institute of Physics of the Chinese Academy of Sciences in Beijing.[17] This Ti:Sa laser source, emitting at 800 nm, is a 350 TW 40 fs facility capable of delivering focused intensities of a few 10^{19} W/cm^2. In our experiment, the delivered intensities and the irradiated targets were changed and in particular we used 10^{17} W/cm^2 and 10^{19} W/cm^2. In the first run at 10^{17} W/cm^2, the laser energy delivered on target was about 200 mJ. The laser beam was focused on target using an F/3 off-axis parabola to a spot with an effective radius $r \leq 50\,\mu$m, at an incidence angle of 22.5° relative to the target normal. An intensity of 10^{17} W/cm^2 is typical of the ps pedestal of PW laser pulses, which is responsible for the creation of the first fast electrons in the pre-plasma already created by the ASE pre-pulse (typically of ns or sub-ns duration). In the second run, at 10^{19} W/cm^2, the focal spot was reduced (the effective laser radius was $r \leq 10\,\mu$m) and the laser energy ranged between 1 J and 3 J. Pre-pulses have been avoided using the optical parametric amplification (OPA) technique.[17]

We used three types of target: (A) simple targets: made of copper of different thickness (10, 25, and 35 μm); (B) two-layer targets: the first one either of plastic or of aluminium with different thickness (15, 40, and 70 μm), the second one (tracer layer) of copper (10 μm); and (C) three-layer targets: the first one of aluminium with different thickness (1, 6, and 10 μm), the second one (tracer layer) of copper (3 μm), and the last one of Al (1 μm). Gold or carbon (100 nm) was added onto the plastic layers on front side to avoid the problem of laser shine-through into the targets. The experimental set-up and the targets design are shown in Fig. 1.

III. DIAGNOSTICS

Several diagnostics were used in the experiment. The position of each diagnostic tool is represented with a vector p(ψ,φ) (see Fig. 1) where $\psi \in [-180°; 180°]$ varies in the horizontal plane (i.e., the equatorial plane), and $\phi \in [-90°; 90°]$, varies with respect to the equatorial plane. p($\psi = 0°, \phi = 0°$) corresponds to the normal to the target front surface.

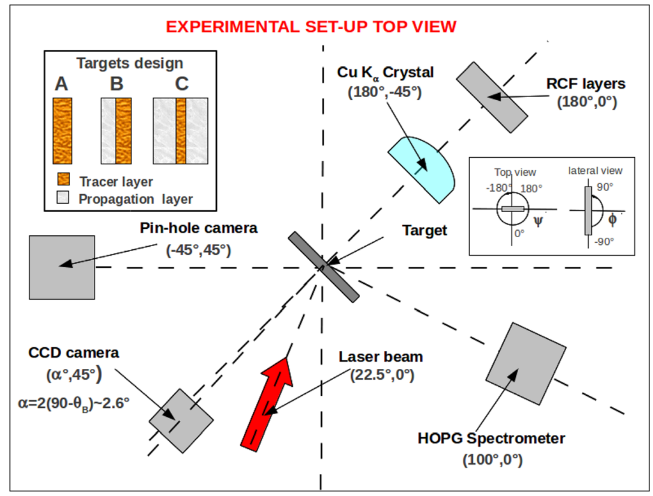

FIG. 1. Top view scheme of the interaction chamber. For all detectors, the position is represented by two angles (ψ, ϕ): ψ varying in the equatorial plane, and φ varying with respect to the equatorial plane. p($\psi = 0°, \phi = 0°$) corresponds to the normal to the target front surface. The inset on the top left shows the three different target designs.

- *X-ray pinhole camera*: A X-ray pinhole camera coupled to a CCD detector was pointed at the front face of the target, where the laser-matter interaction takes place, at the position ($-45°, 45°$) (see Fig. 1). The image magnification of the x-ray spot was 4× and the filter for the CCD detector was 13 μm thick aluminium foil.
- *CR39 track detectors*: CR39 was placed behind the target detecting the ions emitted from the rear face of the target at the position p($180°; 0°$).
- *Shadowgraphy*: A probe beam for shadowgraphy was extracted from the main laser beam, doubled in frequency (400 nm), and sent parallel to the target surface with the goal to verify the formation of plasma as a consequence of the interaction with any pre-pulse. A delay line allowed timing probe beam so that it could arrive to the target between 1 ns before and 250 ps after the main pulse.
- *Highly ordered pyrolytic graphite spectrometer*: Cu$-K_\alpha$ photons are emitted as fast electrons cross the tracer layer; a highly ordered pyrolytic graphite (HOPG) flat X-ray spectrometer has been used to record Cu K-shell spectra with good signal over noise ratio due to the high reflectivity of mosaic graphite crystals. The HOPG spectrometer was tuned to a range of photon energies centered on the Cu $- K_\alpha$ energy. The spectrometer was placed at the rear of the target at the position p($100°; 0°$). An aluminium foil with 14.2 μm thickness preserved the crystal from debris damage.
- *Spherical crystal for X-ray imaging*: Cu $- K_\alpha$ photons are also detected using a spherically bent crystal in the Bragg configuration[26,27] coupled to an X-ray CCD. The spherical crystal combines the refracting properties, typical of a Bragg crystal, to the focusing properties of a spherical mirror. Our crystal is Quartz 2131 with spacing $2\,d = 3.082$ Å as needed to detect Cu K_α photons ($h\nu = 8048$ eV, $\lambda = 1.5406$ Å) at the Bragg angle $\theta_B = 88.6°$ in the second order. The condition of using a nearly 90° Bragg angle comes from the need of reducing

astigmatism in the produced image. The radius of curvature of the crystal is 380 mm giving a focal distance of 190 mm. Hence, we placed the crystal behind the target at a distance of 231 mm at the position p(180°, −45°) obtaining an image onto the CCD placed at 1070 mm at the position p(α, 45°) where $\alpha = 2(90° - \theta_{B°})$. The imaging system magnification is 4.6×. This diagnostic gives a spectrally selected and spatially resolved X-ray image of the K_α spot on target rear side, reproducing the spatial shape of the fast electron beam. In our case, the reached spatial resolution is $\sim 10\,\mu$m. From the obtained images, we can get two types of quantitative informations:

(1) the K_α spot size diameter;
(2) the total K_α signal.

The spot size, measured as a function of target thickness, can be used to evaluate the angle of divergence of the fast electron beam. From the integrated signal as a function of target areal density, it is possible to calculate the fast electrons range for the considered propagation material (plastic, Cu, or Al). Also, with some reasonable assumptions, it is possible to estimate the total energy in the fast electron beam thereby allowing evaluating the conversion efficiency from laser energy into fast electrons.

IV. EXPERIMENTAL RESULTS AT INTENSITY $\sim 10^{17}$ W/cm^2

A. Results

Fig. 2 shows a set of typical $Cu - K_\alpha$ spot images obtained for different targets and different beam energies. Fig. 7 shows the whole set of the experimental results (K_α signal radius (left) and intensity (right)).

$Cu - K_\alpha$ data were not obtained for all targets but only for thinner targets, that is to say: copper 10, 25 and 35 μm, aluminum 15 μm, and plastic 15 and 40 μm. In the obtained images, the monochromatic K_α radiation is embedded into a high noise background. Because of noise, there is an uncertainty in measuring the spot size (FWHM) and the total signal. The average error on the area is about 25%. In some cases (Cu 35 μm in Fig. 2), we observed an annular structure that can also be observed in proton images (see at the end of this section). Such kind of structure has also been observed in previous experiments, for example, those presented in Refs. 27 and 28, and has been described as the result of the possible interplay of the magnetic field created by the hot current and the return ohmic current of background electrons. The images also show similar spot sizes for different thickness of the propagation layer. This behavior is different from most results reported in literature which show divergence and in particular that the K_α spot is always larger then the laser spot size. Our result will be analyzed in detail in the following. The state of the target during the laser irradiation has been checked by using shadowgraphy technique as shown in Fig. 3.

Protons have not been detected in all shots and, when observed, their energy was lower than 1 MeV. In general, a ring structure was visible on the CR39. Such structure could be connected to the action of the pre-pulse which is stronger at the center of the focal spot and weaker at the edge. The breakout of the pre-pulse generated shock does therefore take place before at the spot center and may be strong enough to vaporize the target material, therefore preventing proton acceleration. At the edge, the weaker and slower shock leaves the target intact and here protons can be accelerated.[29]

B. Simulations

In this section, we show results from simulations performed by using a particle in cell code (PIC).[30] The simulations describe the time, space, angular, and energy distribution of a laser-driven electron beam generated by a laser pulse similar to that used in the experiment [50 fs, energy ~ 300 mJ, focused to a 50 μm diameter spot onto aluminium target at intensity $I = 3 \cdot 10^{17}$ W/cm^2 which represents the peak value in time and space (i.e., $\langle I \rangle \sim 10^{17}$ W/cm^2)]. Fig. 4 shows the electron beam: energy distribution as a function of the energy in the Cartesian coordinates (top) and time-angular integrated energy spectrum (bottom).

Fig. 5 shows the evolution of the electron beam angular distribution for different energy ranges. The correlation between angular distribution and energy distribution is clear.

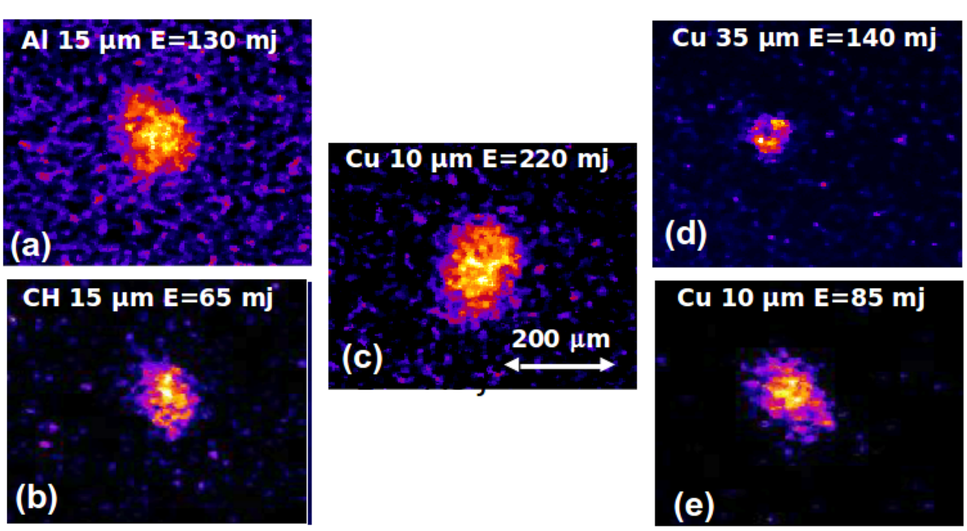

FIG. 2. Typical K_α images obtained during the experimental campaign varying laser energy, target material, and thickness. The images are chosen so to show the effects of changing: the laser energy (c → e), the target material (b → e and a → c), and the target thickness (c → d).

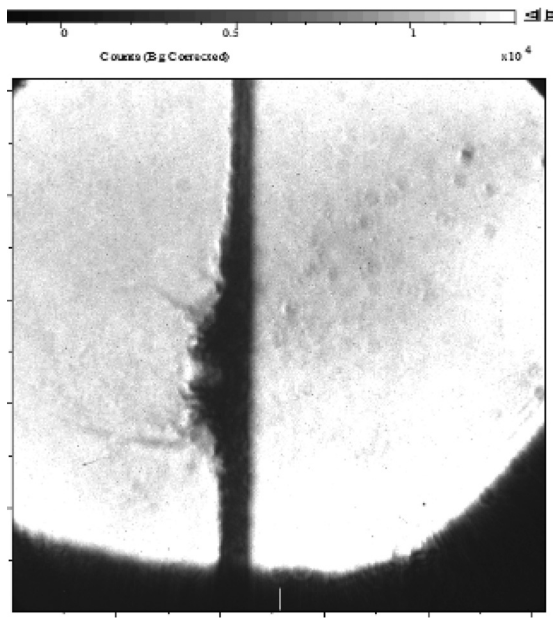

FIG. 3. Image of 25 μm thick Cu target, 250 ps after the laser (E = 130 mJ) was focused on it, as obtained by using shadowgraphy technique. Shadowgraphy results shown that (1) the target surface remains intact until the arrival of the laser (from the left), and (2) the target is not completely destroyed by the laser pulse (this may not be the case for thinner targets).

Indeed increasing the energy the mean FWHM of the angular distribution becomes narrower, and also the electrons are emitted at larger angle with respect to the normal (i.e., $\theta = 0$) as it can be also seen in Fig. 4 (top), that is they more or less follow the laser incidence direction.

The simulations clearly show the presence of "different" electron populations. A majority of hot electrons (E < 50 keV) are characterized by a slope temperature of ~50 keV and they propagate practically perpendicularly to the target surface. Such electrons have relatively low energy and then they have a relatively large initial angular spread $\Delta\theta \sim 26°$, and because of their relatively low energy they are very collisional, which contributes to increase the signal spread as they propagate into the target. Having a very short penetration range, most of these electrons do not contribute much to the K_α signal apart from the case of the thinnest targets or pure copper targets.

Electrons in the high energy range, E > 500 keV, have a propagation at $\langle\theta\rangle \sim 15°$ intermediate between the target normal and the laser direction. Probably, these electrons are produced by a different interaction mechanism (i.e., direct ponderomotive acceleration as compared to resonant-like absorption for slower electrons). These electrons also do not contribute much to K_α signal due to their very low number. Such electrons have a low collision rate due to their high energy and therefore propagate in a rather ballistic way.

Electrons at intermediate energies have an intermediate behavior. The presence of the two main propagation directions is also clear from Fig. 4 (top).

C. Analysis of experimental results

In the literature, the divergence angle of the fast electron beam is typically measured by changing target thickness and measuring the increase of the width of the measured signal

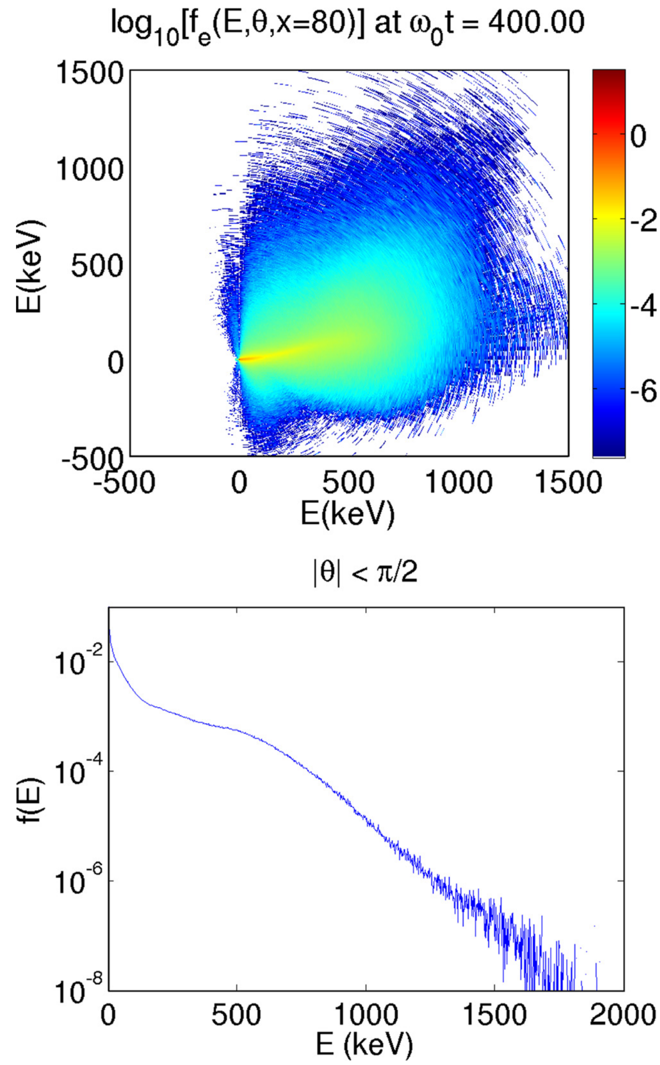

FIG. 4. Energy distribution as a function of the energy Cartesian coordinates (top) and time-angular integrated energy spectrum (bottom) of the fast electron beam, as predicted by the PIC code.

(in general, K_α (Ref. 7) or OTR emission (Ref. 31)). However, our data show a different trend. From the graph in Fig. 7 (left), the spot size seems either to decrease (case of Cu) or to remain approximately constant (case of plastic) with increasing areal density. We believe that this happens because the energy of fast electrons (and so the penetration range) has an angular dependence: The larger the angle from the normal, the smaller the energy of fast electrons. This is confirmed by PIC simulations shown in Sec. IV B and by theoretical investigations (see, for example, Refs. 23 and 32). Therefore, fast electrons propagating in directions far from the normal are stopped before those close to the normal. Then one can expect that for thin targets the signal is due to all electrons, including those which have a large angular spread. For thick targets instead, a "self-filtering" of the electron beam distribution occurs because only faster electrons, characterized by a lower divergence, persist (Fig. 5) and then only those electrons will arrive to the Cu tracer layer. However due to the larger range (and due to the larger target thickness), the spot size may be comparable to the previous one, as schematically shown in Fig. 6. In addition, the large size in thin targets can be justified by the presence of the electron refluxing.

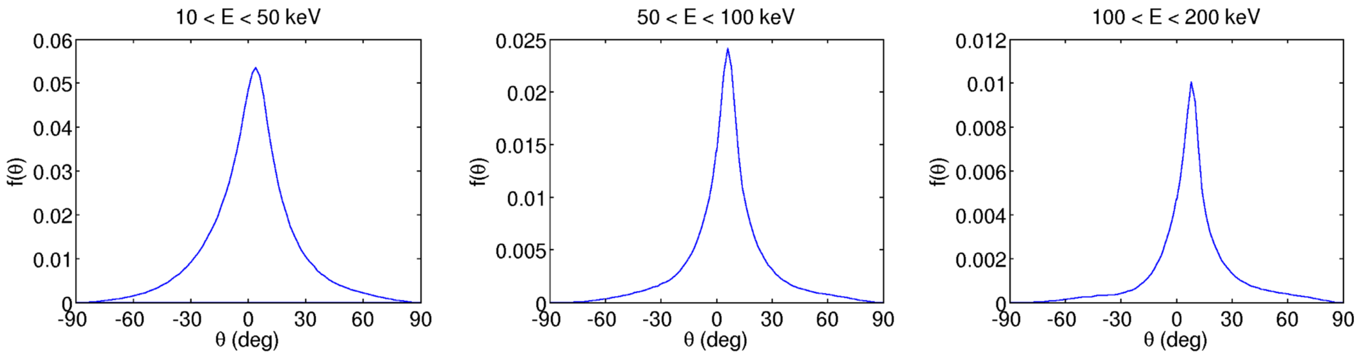

FIG. 5. Evolution of the electron angular distributions for different energy groups (left) $10 < E < 50$ keV, $\langle\theta\rangle \sim 0°$ and $\Delta\theta \sim 26°$, (center) $50 < E < 100$ keV, $\langle\theta\rangle \sim 5°$ and $\Delta\theta \sim 15°$, (right) $100 < E < 150$ keV, $\langle\theta\rangle \sim 10°$ and $\Delta\theta \sim 15°$, as predicted by the PIC code.

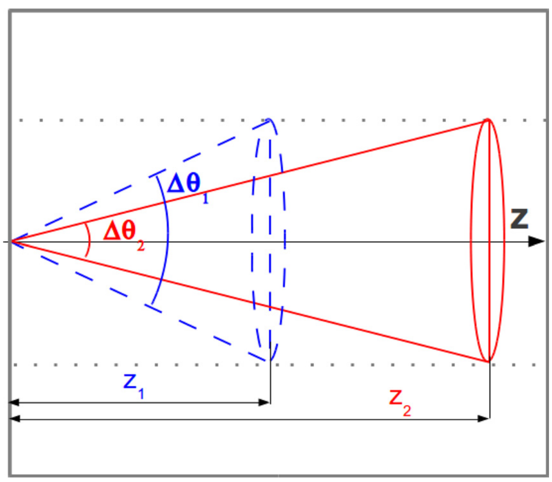

FIG. 6. Simple scheme for electron divergence: The faster electrons (red continuous cone) have lower divergence $\Delta\theta_2$ than the slower ones (blue dashed cone) which are characterized by higher divergence $\Delta\theta_1$. All the electrons contribute to the K_α spot for thin targets z_1, while only faster ones contribute for thicker ones.

Considering the integrated signal as a function of areal density, it is possible to obtain the penetration range for each type of target. With reference to Fig. 7 (right), we obtain the following penetration ranges (i.e., the distance at which the signal is reduced to 1/e of the initial signal):

- copper: $21 \pm 4\,\mu$m or 18.7 ± 3.5 mg/cm^2;
- plastic: $60 \pm 12\,\mu$m or 7.2 ± 1.4 mg/cm^2;
- aluminium: $36 \pm 7\,\mu$m or 9.7 ± 1.9 mg/cm^2.

The obtained ranges are characterized by a mean error of 20% due the interpolation method. This error is reported in Fig. 8 (height of the blue shadowed region).

We analyzed the experimental results by using the model developed in Ref. 23 which describes the electron range as a function of the electron beam temperature T and the target parameters: target temperature T_c, ionization degree Z^*, material (atomic and mass numbers), and conductivity $\sigma(T_c)$. The model account for both collisional and collective effects as well as the electron refluxing in the measurement of the K_α signal (see Appendix). In this run (10^{17} W/cm^2) the electron range is predicted to be less or of the same order of the target thickness then the refluxing effect can be neglected.

We performed our analysis according to the following procedure (which is described in detail in the Appendix):

1. We start from the experimental estimations: (1) the electron penetration range R_{exp} and (2) the total number of collected photons N_{ph}^{ccd}.
2. Knowing the laser pulse temporal and spatial distributions as well as its energy, we calculate the intensity on target and then assuming Beg's[2] or Wilks[33] scaling laws we

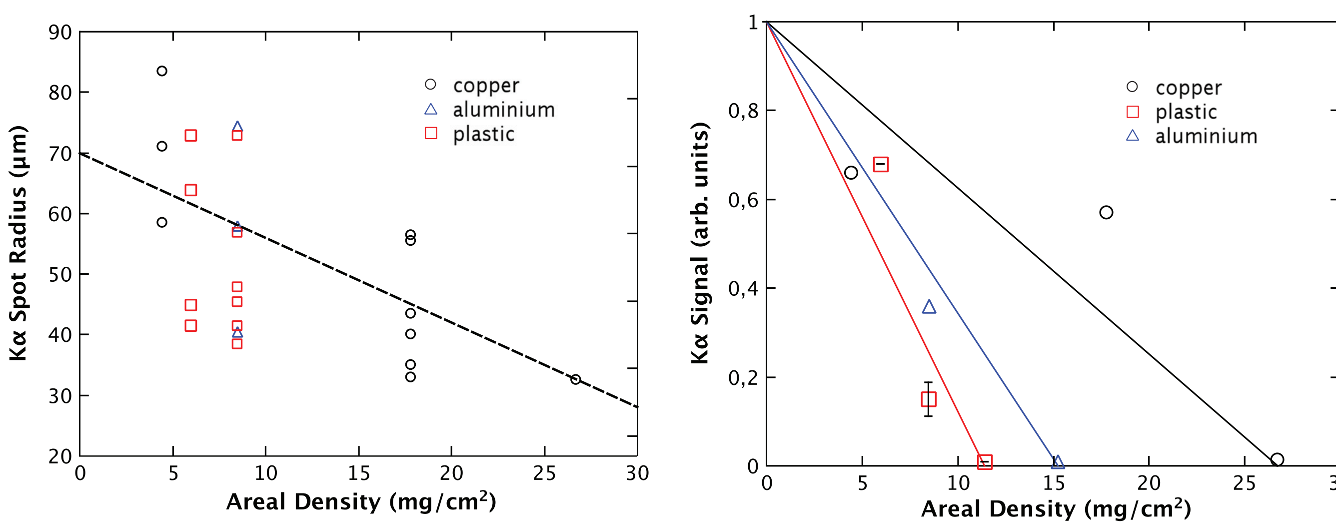

FIG. 7. K_α signal radius (left) and yield (right) for different type of target as a function of the areal density at $I = 10^{17}$ W/cm^2.

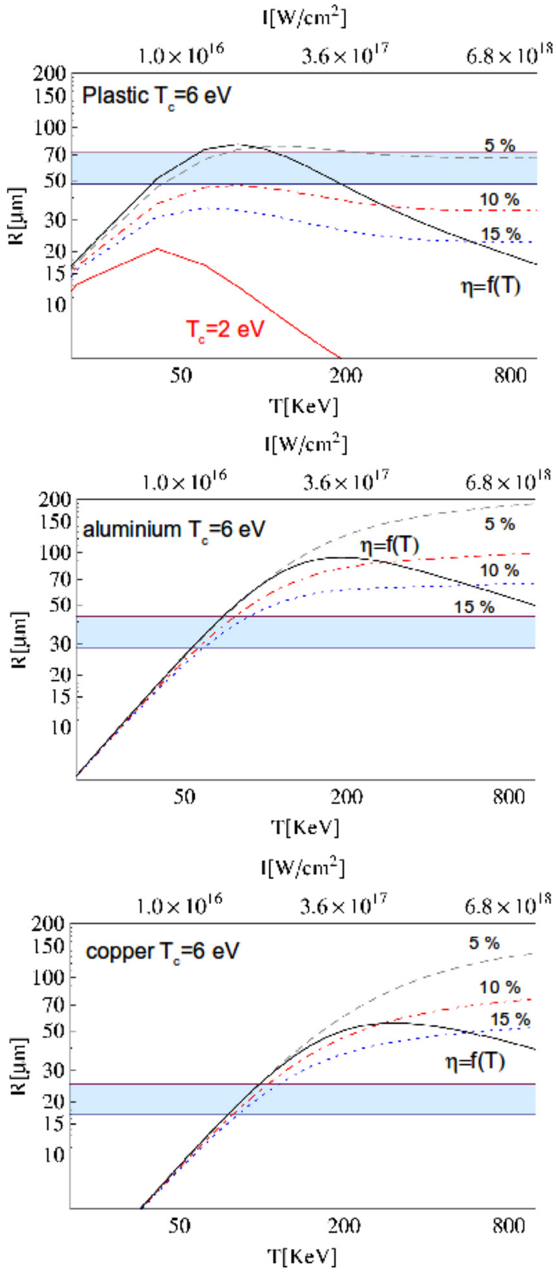

FIG. 8. Theoretical estimation of the total electron penetration range for three different target materials: plastic (top), aluminium (center) and copper (bottom), compared with experimental results (shadowed regions). Theoretical values are calculated at target temperature of 6 eV and three different values of conversion efficiency: 5% (dashed gray), 10% (dotted-dashed red), and 15% (dotted blue). The continuous line is the electron range calculated varying conversion efficiency as a function of laser intensity or electron beam temperature (we use the scaling law proposed by Solodov *et al.*[34]). The red line in the left side picture is the electron beam range in plastic for $T_c = 2$ eV.

estimate the hot electron temperature T (i.e., the average energy over the distribution).

3. By using Eq. (A6), where we insert the experimental value of R_{exp} and of the number of collected K_α photons, we estimate the conversion efficiency η.
4. From η, we estimate the target temperature T_c by assuming that the electron beam energy is transferred uniformly into a cylindrical volume of the target of base $\pi \langle r \rangle^2$ (where $\langle r \rangle$ is the observed K_α spot radius) and of height Min[R_{exp}, Δ_z] (where Δ_z is the target thickness). The choice of cylindrical volume is, in our case, justified by the trends of the experimental data. This allows to estimate the ionization degree and the conductivity of the target at this temperature.
5. From η and T_c we estimate the average electron penetration range $\langle R \rangle$, accounting for both collisional and collective effects.
6. If such range is different from R_{exp}, we modify the electron beam temperature so that $\langle R \rangle = R_{exp}$ for the obtained values of η and T_c and then we repeat the process until the range calculated in step 5 equals R_{exp} for the new set of obtained parameters (T_c and η).

Applying this procedure (from step 1 till 4) to the experimental results, we estimate a target temperature in the range T_c[eV] $\in$ [2,6] and a possible conversion efficiency $\eta(\%) \in [5,15]$. Fig. 8 shows theoretical estimations for the electron penetration range in plastic (top), aluminium (center), and copper (bottom) as a function of the laser intensity (top horizontal axis) or electron beam temperature T (bottom horizontal axis) at target temperature $T_c = 6$ eV for different values of conversion efficiency η (5%, 10%, 15%). These model calculations can be compared to the experimental results (shadowed regions in the plots). Let us notice that, as shown in Fig. 8 (top), the theoretical electron range in plastic calculated at $T_c = 2$ eV (red line) does not match the experimental results (shadowed regions).

Note that in all graphs the change in slope in the function $R = R(T)$ corresponds to the onset of collective effects.

Considering all the physical constraints for all the three target materials, we find a reasonable set of values to be: $T \sim 75$ keV; $T_c \sim 6$ eV, $\eta \sim 5.5\%$ which are compatibles with an intensity $I \sim 4 \times 10^{16}$ W/cm^2 (assuming the cited scaling laws for T[2,33] and η). Such intensity on target is smaller with respect to the initial assumption 10^{17} W/cm^2 but still reasonable taking into account the unavoidable uncertainties in the energy and laser pulse duration measurements on a shot-to-shot basis. Moreover, the estimated conversion efficiency is in agreement with that predicted by previous results; in particular using Solodov scaling law[34] we get $\eta(75\,\text{keV}) \sim 5\%$.

In this range of electron temperatures, the resistive effects are small if compared with collisional ones for Cu and Al. However for plastic, they contribute to reduce the electron range. This is in agreement with other experimental evidences[9,13,35,36] and theoretical investigations[23,32,37] showing that resistive effects start to be relevant at $I(\text{W/cm}^2) \sim 10^{17}$, depending on the type of target. Finally, from the obtained parameters, we estimate the ionization degree and the conductivity of the targets as shown in Table I. The estimation for the hot electron temperature $T \sim 75$ keV supports our view of the electron divergence. Finally, for $T_e = 6$ eV

TABLE I. Ionization degree and conductivity of plastic, aluminium and copper for I = 10^{17} W/cm^2.

$T_c = 6$ eV	Plastic	Aluminium	Copper
Z^*	0.1	3.4	4.8
σ	$1.6 \times 10^5\ \Omega^{-1}\text{m}^{-1}$	$6 \times 10^5\ \Omega^{-1}\text{m}^{-1}$	$5 \times 10^5\ \Omega^{-1}\text{m}^{-1}$

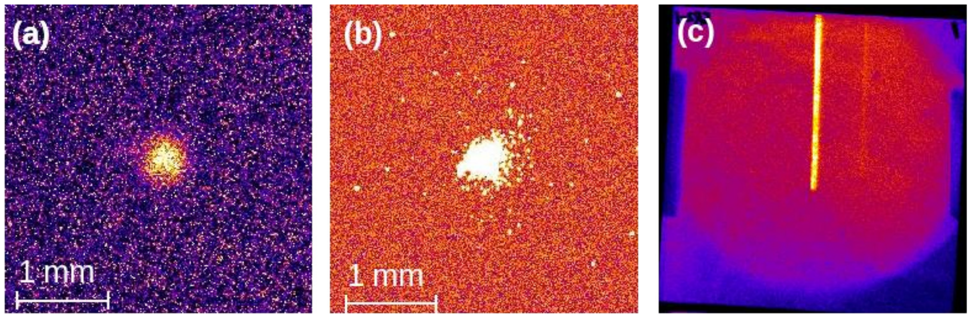

FIG. 9. Typical results obtained with target [Al(1 μm)-Cu(3 μm)-Al(1 μm)], laser energy $E_L = 2.9$ J and intensity $I = 1.8 \times 10^{19}$ W/cm^2. (a) K_α spot, (b) pinhole camera image, and (c) HOPG spectrometer showing the K_α line (integrated signal from 4 successive shots). The K_β line is also visible. The k_α imaging system magnification is X4.6 while the pinhole camera magnification is X4. A 13 μm thick foil was placed in front of the pinhole camera to stop photons below 4 keV.

we estimate the ionization degree and the conductivity of the target for the used materials and the results are shown in Table I.

V. EXPERIMENTAL RESULTS AT INTENSITY $\sim 10^{19}$ W/cm^2

A. Results

In the second run, we focused laser pulses of a few joules in a 10 μm radius spot obtaining an intensity of about 10^{19} W/cm^2. Previous results in literature show that such intensity corresponds to an electron temperature $T \sim 1$ MeV^2. At these temperatures, the fast electron range is expected to be larger than the target thickness (we used targets of types B and C of Fig. 1). This implies the presence of electron refluxing. The K_α yield is hence due to the superposition of different emissions each time the electrons cross the Cu tracer.

Fig. 9 shows a set of typical results (K_α spot size, X-ray pinhole camera image, K_α line from HOPG spectrometer). Fig. 10 shows (left) the K_α signal spot size as a function of the target thickness and (right) the integrated K_α signal as a function of the areal density. Similarly to the previous analysis, the average error on the K_α spot area is about 25%. In this case, no proton signal was detected because the detector had been positioned too far from the target due to setup constraints.

We have estimated the electron penetration length for the different materials using the same method as in the previous run, yielding

- aluminium: 60 ± 12 μm or 16 ± 3 mg/cm^2;
- titanium: 130 ± 26 μm or 116 ± 23 mg/cm^2.

As in the previous analysis, the obtained ranges are characterized by a mean error of 20% due to the interpolation method. This error is reported in Fig. 11 (height of the blue shadowed region).

The trend of the K_α spot size as a function of areal density (Fig. 10, left) suggests that at high intensities the K_α spot size either slowly increases or remains constant. However comparing laser spot size ($\sim$10μm) with the K_α spot size ($\sim$100μm), an electron divergence is expected. A possible explanation is that electron refluxing effect enlarges the spot radius of the obtained K_α images, and this enlargement depends on the ratio between the electron range R and the target thickness Δ_z (i.e., the refluxing number, defined as $n_r = R/\Delta_z$). As shown by some of us in Ref. 23 (Fig. 4, bottom) for a refluxing number sufficiently high the K_α spot radius remains constant as n_r increases. Note that the data obtained at low intensities, shown in Fig. 7, also seemed to show a rather constant or decreasing trend, even if the physical mechanism is different.

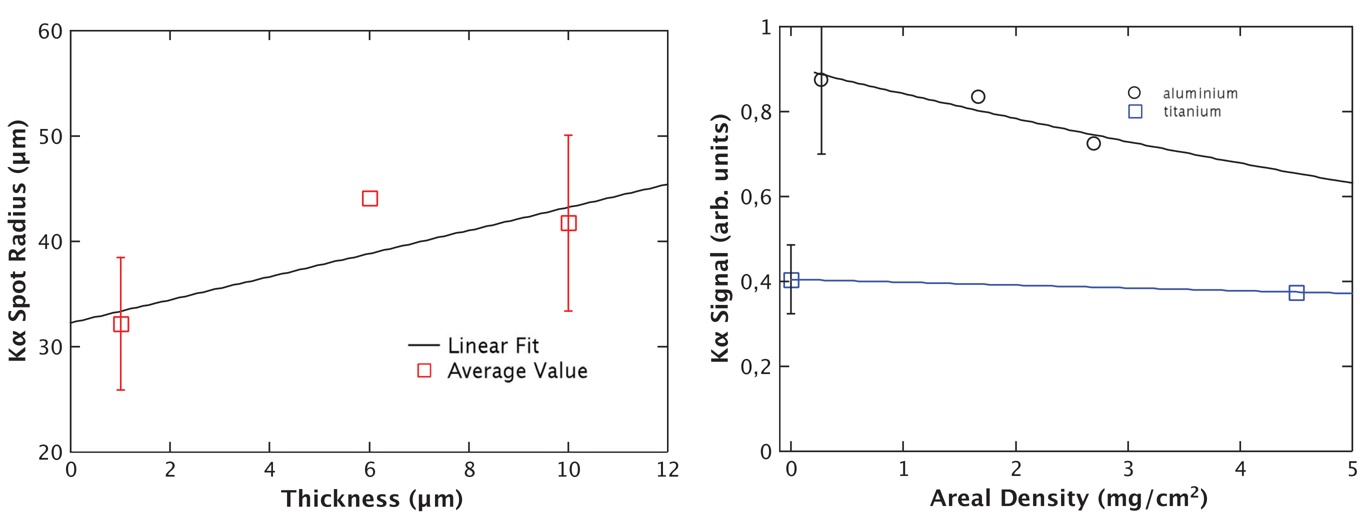

FIG. 10. K_α spot radius (left) and K_α yield (right) for different type of targets as a function of the crossed areal density at I = 10^{19} W/cm^2

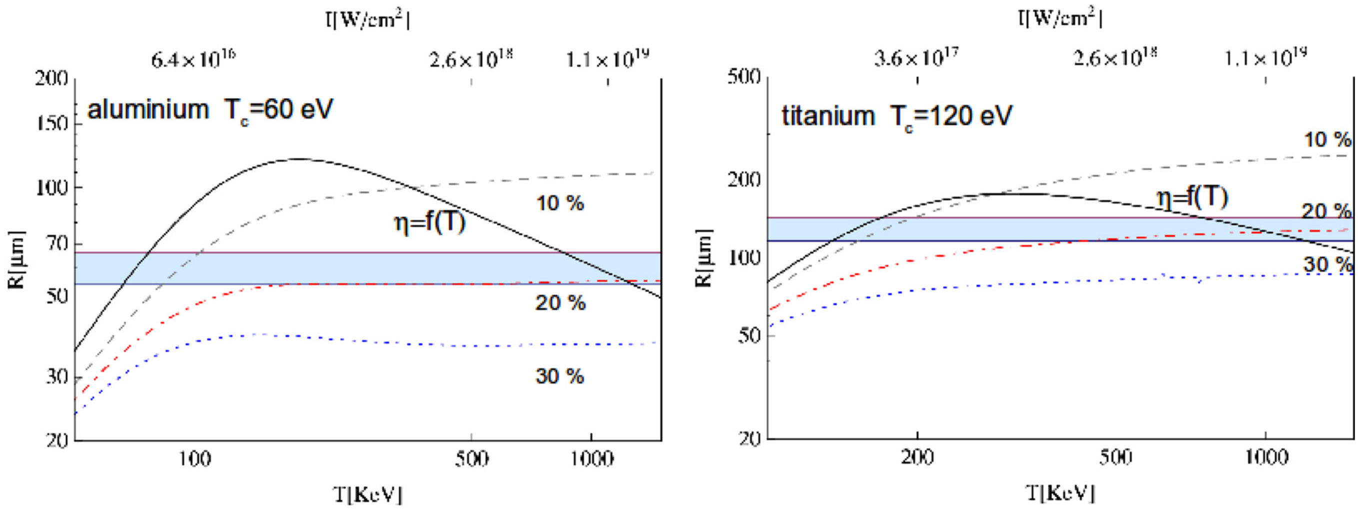

FIG. 11. Theoretical estimations of the total electron penetration range for two different target materials: aluminium (left), and titanium (right) compared with experimental results. Theoretical values are calculated at target temperature of 60 eV (aluminium), 120 eV (titanium), and three different values of efficiencies of conversion: 10% (dashed gray), 20% (dotted-dashed red), and 30% (dotted blue). The continuous line is the electron range calculated varying conversion efficiency as a function of laser intensity according to the scaling law proposed by Solodov *et al.*[34]).

B. Analysis of the experimental results

At intensity 10^{19} W/cm^2, we need to take into account three differences with respect to the analysis of the run at 10^{17} W/cm^2:

- Beg's scaling law is no longer valid. Indeed above 10^{19} W/cm^2 Wilks scaling is probably closed to reality.
- The electric field generated by the charge separation in the target bulk is sufficiently high to slow down the electrons reducing drastically their penetration length (i.e., collective effects are important).
- The expected electron range is larger than the target thickness and electron refluxing effects are important.

Assuming the laser intensity on target to be 10^{19} W/cm^2 and following the procedure explained before, we estimate the conversion efficiency (Eq. (A6)) η to be between 20% and 25% and the target temperature T_c (Eq. (A7)) to be $\sim$60 eV for aluminium and $\sim$120 eV for titanium targets. The higher temperature of titanium is due to the smaller specific heats C (i.e., $T_{Ti}/T_{Al} \sim C_{Al}/C_{Ti} \sim 2$).

Fig. 11 shows the theoretical electron ranges in aluminium (left) at $T_c = 60$ eV and in titanium (right) at $T_c = 120$ eV for different conversion efficiencies: 10% (gray dashed line), 20% (red dotted-dashed line), and 30% (blue dotted). The black continuous line in both graphs represents the electron range calculated by modifying the conversion efficiency as a function of the laser intensity.[2,34] Let us notice that, in principle, there are two possible intersections between the range of experimental results (shadowed regions) and the theoretical values calculated with the model. For instance for the case of *aluminium*, T~50 keV, i.e., collisional dominated regime or T~1000 keV, i.e., collective dominated regime. The first solution gives an estimation of the electron temperature well below the reasonable value for an intensity of 10^{19} W/cm^2. Instead, the solutions in the collective dominated regime are in agreement with known scaling laws. Finally, at T ~1 MeV for both aluminium and titanium, we estimate the ionization degree and the conductivity of the target as shown in Table II.

TABLE II. Ionization degree and conductivity of aluminium and titanium for I = 10^{19} W/cm^2.

	Aluminium (T_c = 60eV)	Titanium (T_c = 120eV)
Z^*	7.8	12
σ	$7.8 \times 10^5\ \Omega^{-1}\text{m}^{-1}$	$1.7 \times 10^6\ \Omega^{-1}\text{m}^{-1}$

VI. CONCLUSIONS

In this paper, we have presented results on laser-driven fast electron propagation for two different intensities (10^{17} W/cm^2 and 10^{19} W/cm^2).

Our experimental results show that the size of the K_α spot size does not seem to vary substantially as a function of target thickness at both the intensities. This shows that indeed the dimension of the K_α spot is determined by a more complex dynamic than just a simple "divergence angle of the fast electron beam." Effects which we describe as "self-filtering" of the fast electron distribution as it propagates in the material may be very important at such intensities. As for the penetration range, varying the intensities in the region where the transition between the dominant collisional effects and dominant electric effects occurs (i.e., $I \in [10^{17}, 10^{19}]$ W/cm^2), we have shown that electric effects start to be important at intensities of the order of 10^{17} W/cm^2, depending on the type of target material and they are dominant over the collisional ones for intensities of the order of 10^{19} W/cm^2. We have also evaluated the temperature, the ionization degree, and the conductivity of the targets. At 10^{17} W/cm^2, temperatures are of the orders of a few eV in all target materials, while at 10^{19} W/cm^2 they are of the order of 100 eV. In both cases, the material reaches the WDM regime at practically solid density (due to the large target thickness and short time scale of the electron heating). We also would like to underline that we have fully explained the two sets of data using our analytical model and identifying two different transport regimes: collisional-dominated for $I \sim 10^{17}$ W/cm^2 and resistive regime for $I \sim 10^{19}$ W/cm^2.

ACKNOWLEDGMENTS

Financial support from MiUR Project PRIN-2009FCC9MS is gratefully acknowledged.

VII. APPENDIX: ANALYSIS METHOD

1. Introduction

This section outlines the method used to analyze the experimental data. K_α images allow to estimate the penetration length and angular divergence of the electron beam. These are "relative" quantities, i.e., they are independent on the detector calibration. Instead, the conversion efficiency of laser light into electrons and the total electron number are "absolute" quantities and then their estimation requires an absolute calibration of the diagnostic system. To analyze such quantities we have used the model developed in Ref. 23, which accounts for both collisional and collective effects on the electric penetration range as well as for electron refluxing in thin foils. The main results of this model are as follows:

- An analytic expression for the average electron range $\langle R \rangle$ as a function of the electron beam temperature T and the target parameters such as background temperature T_c, ionization degree Z^*, material (atomic and mass number) and conductivity $\sigma(T_c)$.
- A geometrical factor π_I accounting for electron refluxing effects in the measurement of the integrated K_α signal.

In particular: The total electron range is given by:[2]

$$R_{tot}(E) = \frac{R_c(E) R_r(E)}{R_c(E) + R_r(E)}, \tag{A1}$$

where R_c is the collisional range (calculated analytically[3,23,38] or extrapolated from the National Institute of Standard and Technology (NIST) database[39]), $R_r(E)$ is the resistive electron range as obtained in Ref. 2. The averaged electron range is calculated as:

$$\langle R \rangle_{tot} = \int_0^\infty R_{tot}(E) f_T(E) dE, \tag{A2}$$

where f_T(E) is the electron beam distribution.[2] The K_α signal modification due to the electron refluxing is accounted for by the geometrical factor π_I. This factor depends on the geometrical properties of the irradiated targets and on the electron beam temperature. Finally, the integrated number of emitted K_α photons N_{ph} is given by

$$N_{ph} = N_{tr} \pi_I, \tag{A3}$$

where $N_{tr} = \omega_k n_i N_h R_{exp}$ is the number of photons emitted by the tracer layer after one transit of the fast electron beam, N_h, n_i and ω_K are, respectively, the total number of electrons crossing the target, the ion density and the K_α fluorescence probability (i.e., the probability that the K-shell ionization is followed by emission of K_α photon).

2. Experimental details

The experimental parameters are as follows:

- $\beta_T = \omega_k n_{tr} \delta_{tr} T_{tr} T_X$; $\beta_O = d\Omega/(4\pi) R_{cry}$; $\beta_D = T_{ccd} Q_E E_{ph}/E_{pe}$.
- Fluorescence probability of Cu K shell (tracer layer) $\omega_k \sim 0.44$.
- Ions density of the tracer layer $n_{tr} = 8 \times 10^{22}$ cm^{-3}.
- Thickness of the tracer layer $\delta_{tr} = 3.10 \times 10^{-4}$ cm.
- Transparency of the tracer layer to the K_α photons $T_{tr} = T_0 \exp\{-\mu_{tr} z\}$ with $\mu = 463$ cm^{-1} for $h\nu = 8.048$ keV.
- Solid angle between interaction point and spherically bent crystal $d\Omega/(4\pi) = 0.5(1 - \cos(\alpha/2))$ where $\alpha = \mathrm{arctg}(r/D)$, and r is the crystal active surface radius and D is the distance between crystal and detector.
- Effective crystal reflectivity $R_{cry} \sim 6.0 \times 10^{-4}$.
- CCD quantum efficiency $Q_E = 0.25$.
- Transmissions of photon flux by the CCD filter $T_{ccd} \sim 0.98$.
- CCD efficiency $E_{ph}/E_{pe} \sim 2205$, which is the ratio between the incident photon energy $E_{ph} = 8.04$ keV and the energy required ($E_{pe} = 3.65$ eV) in order to produce one photo-electron in silicon.

3. Analysis procedure

The K_α signal collected by the detector is given by $N_{ph}^{ccd} = N_{ph} d\Omega/(4\pi) T_{target} R_{cry}$ where T_{target} represents the transmission of the propagation layer (i.e., the portion of the target in which the K_α generated photons propagate), R_{cry} is the effective crystal reflectivity, and $d\Omega/(4\pi)$ is the solid angle of the crystal. The CCD camera signal is given by $X_{ccd} = N_{ph}^{ccd} \beta_D$ where β_D accounts for the CCD response (quantum efficiency)

$$X_{ccd} = \beta N_h R_{exp} \pi_I, \tag{A4}$$

where N_h is the number of hot electrons and $\beta = \beta_t \beta_O \beta_D$ take into account all the experimental parameters (see in the following).

On the other hand, using the energy conservation $N_h \langle E \rangle = \eta E_L$ where E_L is the laser energy and η is the conversion efficiency we can also write

$$X_{ccd} = \beta \eta \frac{E_L}{\langle E \rangle} R_{exp} \pi_I \tag{A5}$$

and the conversion efficiency can be finally obtained as

$$\eta = \frac{1}{\beta} \frac{\langle E \rangle}{E_L} \frac{X_{ccd}}{R_{exp} \pi_I}. \tag{A6}$$

A simple estimation of the temperature reached in the target can be done assuming that the energy of the electron beam is uniformly transferred into the interaction volume, defined as the part of the target occupied by the electron beam (see in the following). The electron beam energy $E_L \eta$ is converted in thermal energy of the target $3/2\,N_e T_c[\mathrm{J}]$. The number of electrons is given by $N_e = n_e$ (cm^{-3}) V_{int} (cm^3) where $n_e = N_A/\mathrm{A}\ \ \rho[\mathrm{g/cc}]\ \ Z^*$ is the electron density, $V_{int}\,[\mathrm{cm}^3] = \pi\langle r\rangle^2\,\mathrm{Min}[R_{exp},\Delta_z]$ represents the interaction volume and $\langle r\rangle$ is the K_{alpha} mean radius. Finally, we obtain:

$$\Delta T[\mathrm{eV}] = 7\times 10^6 \frac{AE_L\eta}{Z^*\rho[\mathrm{g/cc}]V_{int}[\mu\mathrm{m}^3]}. \qquad \text{(A7)}$$

Note that in our specific case the choice of the cylindric volume is supported by the trend observed from the experimental data.

[1]M. Tabak, J. Hammer, M. E. Glinsky, W. L. Kruer, S. C. Wilks, J. Woodworth, E. M. Campbell, M. D. Perry, and R. J. Mason, Phys. Plasmas **1**, 1626 (1994).

[2]F. N. Beg, A. R. Bell, A. E. Dangor, C. N. Danson, A. P. Fews, M. E. Glinsky, B. A. Hammel, P. Lee, P. A. Norreys, and M. Tatarakis, Phys. Plasmas **4**, 447 (1997).

[3]D. Batani, Laser Part. Beams **20**, 321336 (2002).

[4]R. A. Snavely, M. H. Key, S. P. Hatchett, T. E. Cowan, M. Roth, T. W. Phillips, M. A. Stoyer, E. A. Henry, T. C. Sangster, M. S. Singh, S. C. Wilks, A. MacKinnon, A. Offenberger, D. M. Pennington, K. Yasuike, A. B. Langdon, B. F. Lasinski, J. Johnson, M. D. Perry, and E. M. Campbell, Phys. Rev. Lett. **85**, 2945 (2000).

[5]P. K. Patel, A. J. Mackinnon, M. H. Key, T. E. Cowan, M. E. Foord, M. Allen, D. F. Price, H. Ruhl, P. T. Springer, and R. Stephens, Phys. Rev. Lett. **91**, 125004 (2003).

[6]M. H. Key, M. D. Cable, T. E. Cowan, K. G. Estabrook, B. A. Hammel, S. P. Hatchett, E. A. Henry, D. E. Hinkel, J. D. Kilkenny, J. A. Koch, W. L. Kruer, A. B. Langdon, B. F. Lasinski, R. W. Lee, B. J. MacGowan, A. MacKinnon, J. D. Moody, M. J. Moran, A. A. Offenberger, D. M. Pennington, M. D. Perry, T. J. Phillips, T. C. Sangster, M. S. Singh, M. A. Stoyer, M. Tabak, G. L. Tietbohl, M. Tsukamoto, K. Wharton, and S. C. Wilks, Phys. Plasmas **5**, 1966 (1998).

[7]K. B. Wharton, S. P. Hatchett, S. C. Wilks, M. H. Key, J. D. Moody, V. Yanovsky, A. A. Offenberger, B. A. Hammel, M. D. Perry, and C. Joshi, Phys. Rev. Lett. **81**, 822825 (1998).

[8]J. J. Santos, A. Debayle, Ph. Nicola, V. Tikhonchuk, M. Manclossi, D. Batani, A. Guemnie-Tafo, J. Faure, V. Malka, and J. J. Honrubia, Phys. Plasmas **14**, 103107 (2007).

[9]F. Pisani, A. Bernardinello, D. Batani, A. Antonicci, E. Martinolli, M. Koenig, L. Gremillet, F. Amiranoff, S. Baton, J. Davies, T. Hall, D. Scott, P. Norreys, A. Djaoui, C. Rousseaux, P. Fews, H. Bandulet, and H. Pepin, Phys. Rev. E **62**, R5927 (2000).

[10]T. A. Hall, S. Ellwi, D. Batani, A. Bernardinello, V. Masella, M. Koenig, A. Benuzzi, J. Krishnan, F. Pisani, A. Djaoui, P. Norreys, D. Neely, S. Rose, M. H. Key, and P. Fews, Phys. Rev. Lett. **81**, 1003 (1998).

[11]M. Manclossi, J. J. Santos, D. Batani, J. Faure, A. Debayle, V. T. Tikhonchuk, and V. Malka, Phys. Rev. Lett. **96**, 125002 (2006).

[12]J. J. Santos, D. Batani, P. McKenna, S. D. Baton, F. Dorchies, A. Dubrouil, C. Fourment, S. Hulin, Ph. Nicolalai, M. Veltcheva, P. Carpegiani, M. N. Quinn, E. Brambrink, M. Koenig, M. Rabec Le Glohaec, Ch. Spindloe, and M. Tolley, Plasma Phys. Controlled Fusion **51**, 014005 (2009).

[13]B. Vauzour, J. J. Santos, A. Debayle, S. Hulin, H.-P. Schlenvoigt, X. Vaisseau, D. Batani, S. D. Baton, J. J. Honrubia, Ph. Nicola, F. N. Beg, R. Benocci, S. Chawla, M. Coury, F. Dorchies, C. Fourment, E. d'Humieres, L. C. Jarrot, P. McKenna, Y. J. Rhee, V. T. Tikhonchuk, L. Volpe, and V. Yahia, "Relativistic high-current electron-beam stopping-power characterization in solids and plasmas: Collisional versus resistive effects," Phys. Rev. Lett. **109**, 255002 (2012).

[14]D. Batani, W. Nazarov, T. Hall, T. Lwer, M. Koenig, B. Faral, A. Benuzzi-Mounaix, and N. Grandjouan, Phys. Rev. E **62**, 8573 (2000).

[15]D. Batani, S. D. Baton, M. Manclossi, J. J. Santos, F. Amiranoff, M. Koenig, E. Martinolli, A. Antonicci, C. Rousseaux, M. Rabec Le Gloahec, T. Hall, V. Malka, T. E. Cowan, J. King, R. R. Freeman, M. Key, and R. Stephens, Phys. Rev. Lett. **94**, 055004 (2005).

[16]F. Pèrez, A. Debayle, J. Honrubia, M. Koenig, D. Batani, S. D. Baton, F. N. Beg, C. Benedetti, E. Brambrink, S. Chawla, F. Dorchies, C. Fourment, M. Galimberti, L. A. Gizzi, L. Gremillet, R. Heathcote, D. P. Higginson, S. Hulin, R. Jafer, P. Koester, L. Labate, K. L. Lancaster, A. J. MacKinnon, A. G. MacPhee, W. Nazarov, P. Nicolai, J. Pasley, R. Ramis, M. Richetta, J. J. Santos, A. Sgattoni, C. Spindloe, B. Vauzour, T. Vinci, and L. Volpe, Phys. Rev. Lett. **107**, 065004 (2011).

[17]Z. Wang, C. Liu, Z. Shen, Q. Zhang, H. Teng, and Z. Wei, Opt. Lett. **36**, 3194–3196 (2011).

[18]A. R. Bell, J. R. Davies, S. Guerin, and H. Ruhl, Plasma Phys. Controlled Fusion **39**, 653 (1997).

[19]V. T. Tickhonchuk, Phys. Plasmas **9**, 1416–1421 (2002).

[20]E. Martinolli, M. Koenig, S. D. Baton, J. J. Santos, F. Amiranoff, D. Batani, E. Perelli-Cippo, F. Scianitti, L. Gremillet, R. Mlizzi, A. Decoster, C. Rousseaux, T. A. Hall, M. H. Key, R. Snavely, A. J. MacKinnon, R. R. Freeman, J. A. King, R. Stephens, D. Neely, and R. J. Clarke, Phys. Rev. E **73**, 046402 (2006).

[21]P. Neumayer, B. Aurand, M. Basko, B. Ecker, P. Gibbon, D. C. Hochhaus, A. Karmakar, E. Kazakov, T. Khl, C. Labaune, O. Rosmej, An. Tauschwitz, B. Zielbauer, and D. Zimmer, Phys. Plasmas **17**, 103103 (2010).

[22]M. N. Quinn, X. H. Yuan, X. X. Lin, D. C. Carroll, O. Tresca, R. J. Gray, M. Coury, C. Li, Y. T. Li, C. M. Brenner, A. P. L. Robinson, D. Neely, B. Zielbauer, B. Aurand, J. Fils, T. Kuehl, and P. McKenna, Plasma Phys. Controlled Fusion **53**, 025007 (2011).

[23]L. Volpe, D. Batani, A. Morace, and J. J. Santos, Phys. Plasmas **20**, 013104 (2013).

[24]D. Batani, J. R. Davies, A. Bernardinello, F. Pisani, M. Koenig, T. A. Hall, S. Ellwi, P. Norreys, S. Rose, A. Djaoui, and D. Neely, Phys. Rev. E **61**, 5725 (2000).

[25]J. Myatt, W. Theobald, J. A. Delettrez, C. Stoeckl, M. Storm, T. C. Sangster, A. V. Maximov, and R. W. Short, Phys. Plasmas **14**, 056301 (2007).

[26]A. Morace and D. Batani, Nucl. Instrum. Methods Phys. Res. A **623**, 797 (2010).

[27]J. A. Koch, M. H. Key, R. R. Freeman, S. P. Hatchett, R. W. Lee, D. Pennington, R. B. Stephens, and M. Tabak. Phys. Rev. E **65**, 016410 (2001).

[28]P. A. Norreys, J. S. Green, J. R. Davies, M. Tatarakis, E. L. Clark, F. N. Beg, A. E. Dangor, K. L. Lancaster, M. S. Wei, M. Zepf, and K. Krushelnick, Plasma Phys. Controlled Fusion **48**(2), L11 (2006).

[29]F. Lindau, O. Lundh, A. Persson, P. McKenna, K. Osvay, D. Batani, and C.-G. Wahlstrm, Phys. Rev. Lett. **95**, 175002 (2005).

[30]E. Lefebvre, N. Cochet, S. Fritzler, V. Malka, M.-M. Aleonard, J.-F. Chemin, S. Darbon, L. Disdier, J. Faure, and A. Fedotoff, Nucl. Fusion **43**, 629 (2003).

[31]J. J. Santos, F. Amiranoff, S. D. Baton, L. Gremillet, M. Koenig, E. Martinolli, M. Rabec Le Gloahec, C. Rousseaux, D. Batani, A. Bernardinello, G. Greison, and T. Hall, Phys. Rev. Lett. **89**, 025001 (2002).

[32]A. Debayle, J. J. Honrubia, E. d'Humires, and V. T. Tikhonchuk, Phys. Rev. E **82**, 036405 (2010).

[33]S. C. Wilks, W. L. Kruer, M. Tabak, and A. B. Langdon, Phys. Rev. Lett. **69**, 1383 (1992).

[34]A. A. Solodov, K. S. Anderson, R. Betti, V. Gotcheva, J. Myatt, J. A. Delettrez, S. Skupsky, W. Theobald, and C. Stoeckl. Phys. Plasmas **16**, 056309 (2009).

[35]B. Vauzour, Ph.D. thesis, University of Bordeaux, 2012.

[36]J. J. Santos, S. Hulin, B. Vauzour, X. Vaisseau, D. Batani, R. Bouilleaud, F. Deneuville, F. Dorchies, J.-L. Feugeas, C. Fourment, E. dHumires, Ph. Nicolai, V. T. Tikhonchuk, M. Touati, A. Debayle, J. J. Honrubia, L. Gremillet, T. Ceccotti, V. Floquet, R. Benocci, A. Morace, M. Veltcheva, L. Volpe, S. D. Baton, F. Prez, H.-P. Schlenvoigt, V. Yahia, F. N. Beg, S. Chawla, L. C. Jarrot, J. Peebles, H. Sawada, A. Sorokovikova, M. Wei, R. Fedosejevs, S. Kerr, M. Coury, R. Gray, P. McKenna, K. Li, J. R. Davies, Y. Rhee, H. McLean, and P. Patel, in 39th EPS-PPD Conference, Stockholm, July 2012.

[37]A. Debayle and V. T. Tikhonchuk, Phys. Plasmas **14**, 073104 (2007).

[38]C. Deutsch, H. Furukawa, K. Mima, and K. Nishihara, Phys. Rev. Lett. **77**, 2483 (1996).

[39]See http://physics.nist.gov/PhysRefData/Star/Text/ESTAR.html for electron range data.